Ionics (2018) 24:363–372
DOI 10.1007/s11581-017-2200-0

ORIGINAL PAPER

Fabrication and electrochemical investigation of MWO_4 (M = Co, Ni) nanoparticles as high-performance anode materials for lithium-ion batteries

Xi-Xin Wang[1] · **Yang Li**[1] · **Mao-Cheng Liu**[1,2] · **Ling-Bin Kong**[1,2]

Received: 28 March 2017 / Revised: 12 June 2017 / Accepted: 18 June 2017 / Published online: 7 July 2017

Abstract In this work, the MWO_4 (M = Co, Ni) nanoparticles were successfully synthesized by a facile one-step hydrothermal method and used as novel anode materials for LIBs. The micromorphology of obtained $CoWO_4$ and $NiWO_4$ was uniform nanoparticles with the size of ~60 and ~40 nm, respectively, by structural characterization including X-ray diffraction (XRD), scanning electron microscopy (SEM), and transmission electron microscopy (TEM). When tested as lithium-ion battery anode, $CoWO_4$ nanoparticles exhibited a stabilized reversible capacity of 980 mA h g^{-1} at 200 mA g^{-1} after 120 cycles and 632 mA h g^{-1} at 1000 mA g^{-1} even after 400 cycles. And, the discharge capacity was as high as 550 mA h g^{-1} at the 400th cycle for $NiWO_4$ nanoparticles. The excellent electrochemical performance could be attributed to the unique nanoparticles structure of the materials, which can not only shorten the diffusion length for electrons and lithium ions but also provide a large specific surface area for lithium storage.

Keywords Tungstate · Anode material · Hydrothermal synthesis · Reversible capacity · Li-ion batteries

✉ Ling-Bin Kong
konglb@lut.cn

[1] State Key Laboratory of Advanced Processing and Recycling of Non-ferrous Metals, Lanzhou University of Technology, Lanzhou 730050, People's Republic of China

[2] School of Materials Science and Engineering, Lanzhou University of Technology, Lanzhou 730050, People's Republic of China

Introduction

As persistent increase in the requirement for clean energy, people pay close attention to multifarious electrochemical energy storage, especially lithium-ion batteries (LIBs), has been widely used in digital products such as cellphones and laptops, also reveal hopeful application in electromobile [1–6]. The requirements for these applications are quite stringent, so more excellent performance for prospective LIBs electrodes [7–9]. Currently, commercial LIB anodes are made by graphite, but the low energy density and security issues during use limits its further development [1, 10–12]. As a consequence, we need seek replaceable electrode materials which can satisfy the future electrode materials.

In recent years, tungsten (W) involved in materials such as oxides, nitrides, and oxysalts also has already been proven to be feasible for electrochemical energy storage, because of high specific capacity, low working voltage, abundant reserves, and environmental friendliness. In addition, metal tungstate as an independent entity, such as $FeWO_4$ [13], $MnWO_4$ [14, 15], and $ZnWO_4$ [16] reveals excellent electrochemical performance on account of the synergistic effect of different metal elements. Among them, cobalt tungstate ($CoWO_4$) and nickel tungstate ($NiWO_4$) have been researched as promising replacements for catalysis [17], dielectric ceramics [18], oxygen-evolving electrocatalysts [19], and supercapacitors [20–22]. However, research on the electrochemical capability for LIBs has rarely been reported. As similar to most negative electrode materials, metal tungstate materials also contain a commonality of large volume expansion, which results in poor reversible capacity and cyclability. To overcome the flaw, the most common and effective method is to project various nanostructures, such as nanoparticles [23], nanowires [24], and hollow structures [25, 26], which can effectively reduce the capacity decay by relieving volume

expansion during Li^+ insertion and extraction. In addition, the nanostructured electrode with the advantage of small size, large specific surface area, and high diffusion coefficient of atoms greatly enhances the reactivity of electrode reaction and increases the reversible capacity of the active material [27].

Hence, the $CoWO_4$ and $NiWO_4$ with the structure of uniform monodisperse nanoparticles have been successfully synthesized by a facile one-step hydrothermal method. And, as far as we know, this is the first report on $CoWO_4$ and $NiWO_4$ nanoparticles for application as LIB anode. The unique nanostructure effectively increases the reaction site, reduces the volume expansion effect, and maintains the stability of the electrode structure during Li ion insertion and extraction. Inspiringly, the $CoWO_4$ and $NiWO_4$ electrodes all demonstrate excellent electrochemical performance with high reversible capacity, good cycle performance, and rate capability.

Experimental

Synthesis of materials

As in a traditional hydrothermal reaction, 2 mmol of $NaWO_4{\cdot}2H_2O$ was added in 40 mL of distilled water. And, 2 mmol of Co $(NO_3)_2{\cdot}6H_2O$ (or 2 mmol of Ni $(NO_3)_2{\cdot}6H_2O$) was also added in 40 mL of distilled water, which was dropwise added in the above $NaWO_4$ solution under magnetic stirring and continued stirring for 30 min after titration. Then, the mixed solution was transferred into a 100-mL Teflon-lined stainless-steel autoclave and maintained in the stove at 180 °C for 8 h. The obtained products were washed repeatedly by distilled water and absolute ethanol, and finally dried at 80 °C in an oven.

Characterization of materials

The products were characterized by power X-ray diffraction measurements (XRD, Rigaku, D/MAX 2400, Japan), X-ray photoelectron spectroscopy (XPS, ESCALAB250xi), scanning electron microscopy (SEM) (JEOL, JSM-6701F, Japan) with energy dispersive spectrometer (EDS), and transmission electron microscopy (TEM) (JEOL, JEM-2010, Japan).

Electrochemical measurements

The button cells were used to test the electrochemical property of the $CoWO_4$ and $NiWO_4$ samples. The electrode included 10 wt% of the sodium alginate binder, 20 wt% of the acetylene black, and 70 wt% of the active material. The slurry evenly dispersed on the copper foil by coater with 100 μm thickness and transferred to the 60 °C drying oven for 8 h. Then, the copper foil after tableting and made it into wafers of 14 mm diameter by a puncher, then put them in a 120 °C vacuum oven for 10 h. The Li wafers were used as the counter electrode and 1 M $LiPF_6$ in EC-DMC (1:1 by volume) as the electrolyte. The electrochemical properties of the obtained cells were tested on a LAND CT2001A system. And, the cyclic voltammetry (CV) and electrochemical impedance spectra (EIS) was tested on an electrochemical workstation (CHI660C).

Results and discussion

Structural analysis

The crystallographic structures of the MWO_4 (M = Co, Ni) were further authenticated by X-ray diffraction (XRD). The diffraction patterns (Fig. 1a) are at 2θ = 30.480°, 53.880°, and 64.840°, corresponding to ($\bar{1}$ 11), ($\bar{1}$22), and ($\bar{2}$31), respectively. Other sharper peaks also can match well to the standard $CoWO_4$ phase (JCPDS card no. 15-0867). As shown in Fig. 1b, the $NiWO_4$ samples we obtained are amorphous material, which can be proved by the broad and weak XRD patterns (blue line). But, after annealing at 600 °C for 1 h, the peaks (orange line) became sharper and stronger. Three of the strongest peaks at 2θ = 30.920°, 24.880°, and 54.640° are attributed to ($\bar{1}$11), (022), and ($\bar{2}$ 02) facts according to the pure-phase $NiWO_4$ (JCPDS card no. 15–0755), respectively. In addition, no impurity peaks can be found in both XRD patterns of $CoWO_4$ and $NiWO_4$ samples. These consequences reveal that the $CoWO_4$ and $NiWO_4$ with high purity and crystallinity have been successfully synthesized.

The micromorphology of the MWO_4 (M = Co, Ni) is shown in Fig. 2 by SEM, and the EDS attached to SEM confirmed the chemical constitution. The low-magnification SEM images of $CoWO_4$ and $NiWO_4$ nanostructures are shown in Fig. 2a, c, respectively. Evidently, two tungstate nanoparticles reveal similar micromorphology. The $CoWO_4$ nanoparticles show unordered accumulation of relatively uniform particles with a size of 50–100 nm, which can be proved by the high-magnification SEM image (Fig. 2b). The $NiWO_4$ nanoparticles also can be clearly visible in the high-magnification SEM image (Fig. 2d), similar but smaller than $CoWO_4$ nanoparticles, with a size of 30–50 nm. The uniform nanoparticles can effectively promote the formation of stabilized solid electrolyte interphase (SEI) layer and increase reversible capacity. In addition, the energy-dispersive X-ray spectroscopy (EDS) analyses (Fig. 2e, f) also testifies the existence of Co, W, O, and Ni, W, and O elements, respectively, which further confirmed that the samples are mainly made of $CoWO_4$ or $NiWO_4$.

Figure 3 shows the TEM and HRTEM images of $CoWO_4$ and $NiWO_4$ nanoparticles. The TEM images as shown in Fig. 3a, b reveal that the different $CoWO_4$ (or $NiWO_4$)

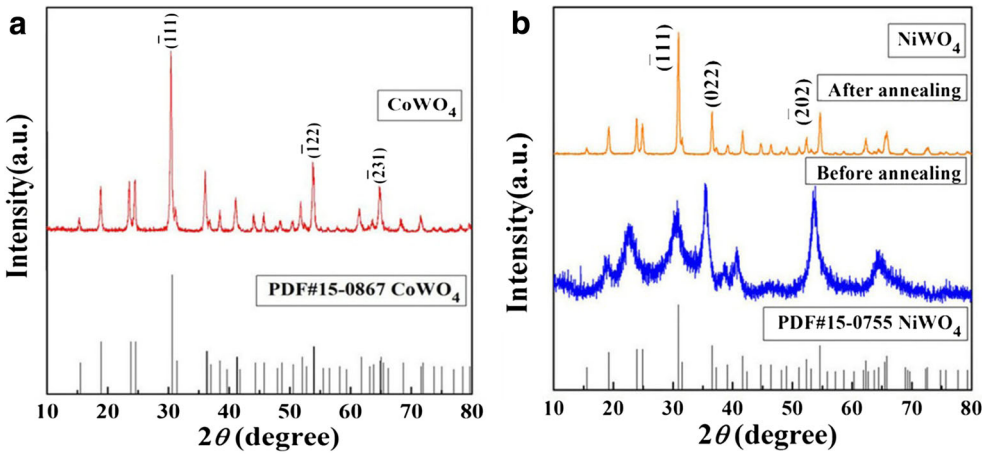

Fig. 1 XRD patterns of $CoWO_4$ (**a**) and $NiWO_4$ (**b**) $NiWO_4$ samples

nanoparticles are similar in size and morphology. It is obvious that the obtained $CoWO_4$ and $NiWO_4$ are crystalline nanoparticles with the single particle size of about 40–60 nm, which conform to the conclusion of the SEM images. Two tungstate nanoparticles are attained to the size of the mesoporous materials, which can improve cycle performance by relieving the tension caused by repeated Li^+ insertion and extraction and avoiding the abscission of electrode materials. On the other

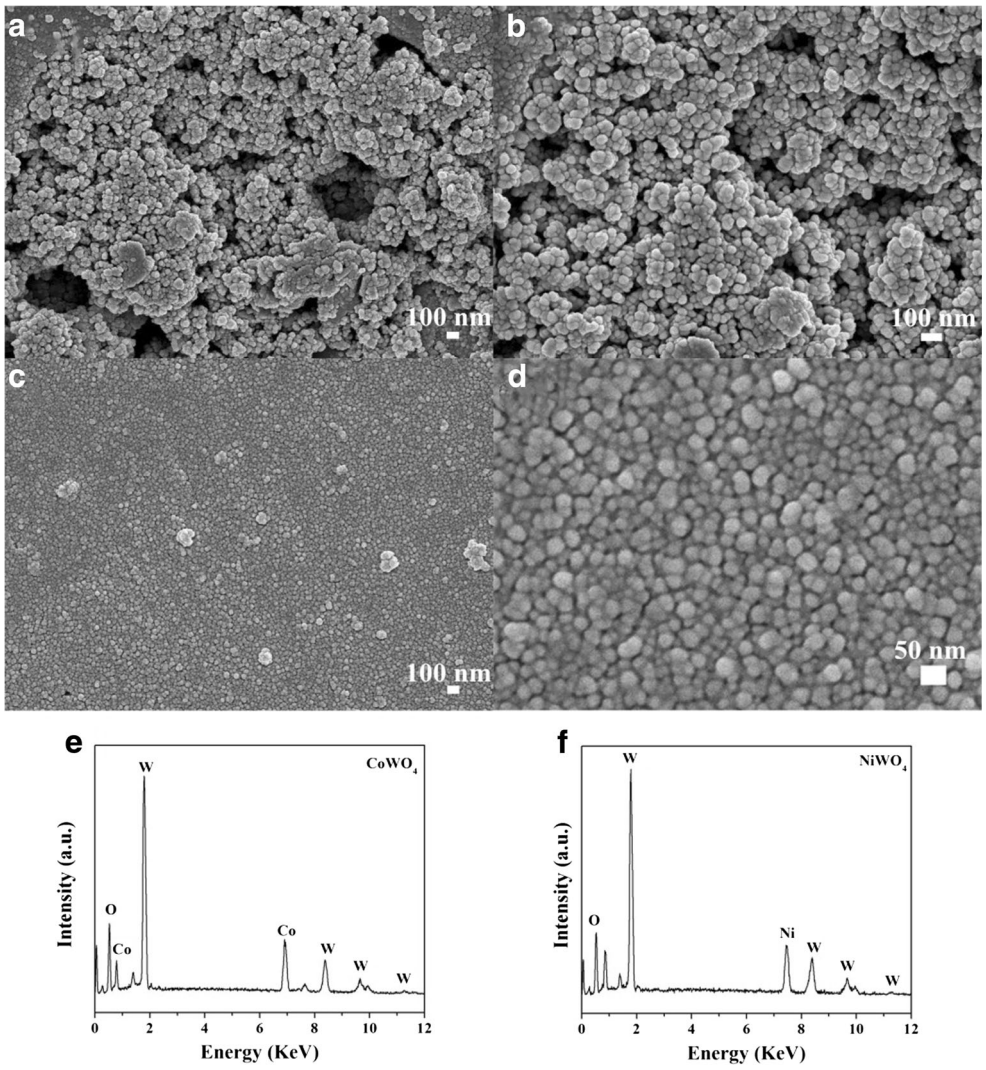

Fig. 2 SEM images of $CoWO_4$ (**a**, **b**). SEM images of $NiWO_4$ (**c**, **d**). EDS spectrum of $CoWO_4$ and $NiWO_4$ (**e**, **f**)

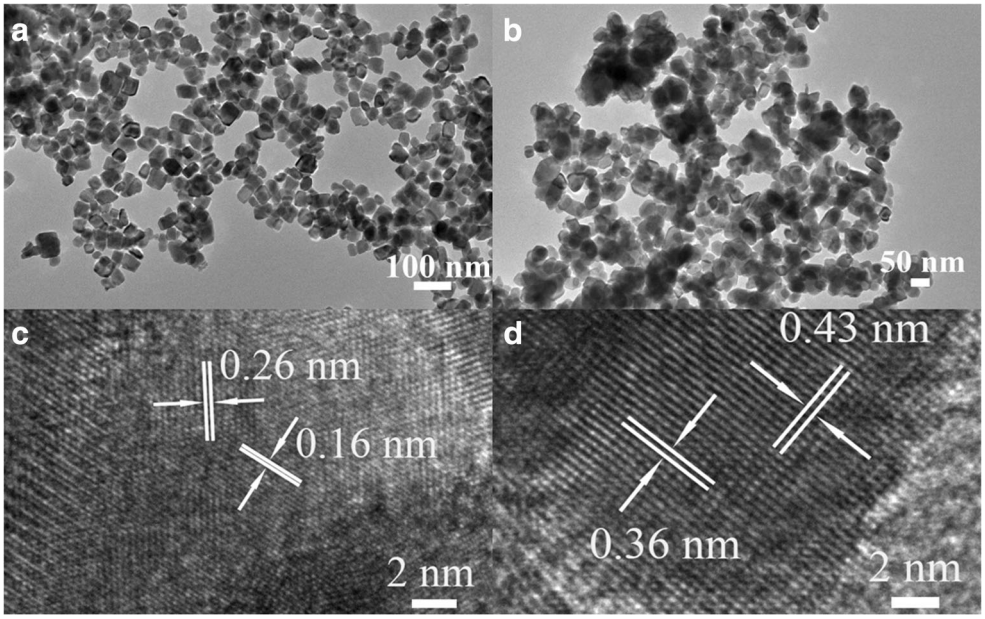

Fig. 3 TEM and HRTEM images of $CoWO_4$ (**a**, **c**). TEM and HRTEM images of $NiWO_4$ (**b**, **d**)

hand, the nanoparticle structure can shorten the diffusion distance of electrons and lithium ions and increase electrochemical reaction sites to enhance the rate capability. In addition, the HRTEMs image (Fig. 3c) also can show clear lattice fringes separated by 0.16 and 0.26 nm, corresponding to the (212) and (002) crystal facets of $CoWO_4$, respectively. And, in the HRTEMs image of $NiWO_4$ (Fig. 3d), the (011) and (001) crystal facets exactly correspond to the d-spacing of 0.36 and 0.43 nm, respectively.

Electrochemical testing

To explore the electrochemical performances of the $CoWO_4$ and $NiWO_4$ nanoparticles, the CV tests (Fig. 4) were earliest implemented, at a scan rate of 0.1 mV s^{-1} within the voltage range from 0.01 to 3.0 V. As shown in the original discharge process of $CoWO_4$ (Fig. 4a), the obvious reduction peaks are revealed at ~1.2, ~0.5, and ~0.25 V, which are possibly corresponded to the reduction of $CoWO_4$ to Co(0), W(0), and the formation of the amorphous Li_2O, as can be explained by Eq. (1) [13–15, 28–31]:

$$CoWO_4 + 8\,Li^+ + 8\,e^- \rightarrow Co + W + 4\,Li_2O \quad (1)$$

The reduction peaks of subsequent cycles move to ~1.75 and ~0.25 V because of the break of the $CoWO_4$ structures and the formation of SEI layer. Furthermore, two broad oxidation peaks in the charging process appear at around 1.1–1.4 V, corresponding to the reversible conversion of Co and W into CoO and WO_3. In the subsequent cycles, the potentials of redox peaks remain unchanged, which can be explained by the reversible reaction in Eq. (2) [13–15, 28–31]:

$$Co + W + 4\,Li_2O \leftrightarrow CoO + WO_3 + 8\,Li^+ + 8\,e^- \quad (2)$$

On the other hand, later redox peaks overlap very well, indicating the good reversibility of the lithium storage of the

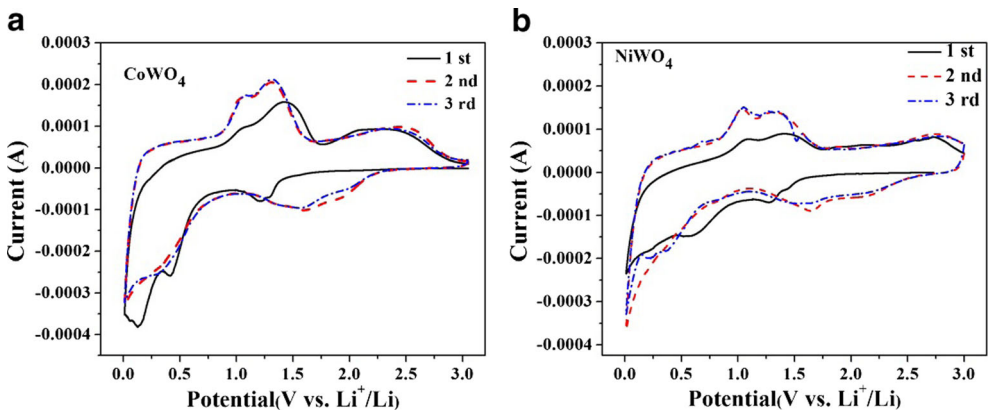

Fig. 4 CV curves of the $CoWO_4$ (**a**) and $NiWO_4$ (**b**) electrode

$CoWO_4$ electrode. In addition, the CV curve of $NiWO_4$ electrode (Fig. 4b) is similar to that of the $CoWO_4$ electrode; the only difference is the potentials of the redox peaks.

In order to confirm the formation of Co, W, CoO, and WO_3 during the process of discharge/charge, the study of XPS was carried out to distinguish the valence state of the $CoWO_4$ electrode material, which is shown in Fig. 5. Figure 5a, b shows the XPS spectra of the fresh prepared electrode of the $CoWO_4$ nanoparticles. Two strong peaks at binding energies (B.E.s) = 781.08 and 797.5 eV are attributed to Co^{2+} $2p_{3/2}$ and Co^{2+} $2p_{1/2}$, respectively. The W 4f spectra shows two peaks at B.E. = 35.18 and 37.28 eV, corresponding to $4f_{7/2}$ and $4f_{5/2}$, respectively. These values of B.E.s can be used to verify the as-synthesized $CoWO_4$ nanoparticles and indicate that the elements of Co and W exist in Co^{2+} and W^{6+}, respectively [19, 20].

In order to clarify the electrochemical processes during the cyclic process, the ex-situ XPS was also tested after the electrode discharge/charge at a current density of 200 mA g^{-1} for one cycle. As shown in Fig. 5c, the peaks belonging to Co $2p_{3/2}$ and Co $2p_{1/2}$ transform into two parts. The retention of the Co^{2+} $2p_{3/2}$ and Co^{2+} $2p_{1/2}$ peaks is due to the oxidation reaction of Co in the charging process. Besides the existence of Co^{2+}, two peaks at B.E. = 778.0 and 793.3 eV correspond to the Co^0 state, which indicates that Co element exists partially in the metallic after one circle, and it also confirms that the oxidation process of Co element is incomplete because of high current density [32]. Furthermore, the appearance of W^0 $4f_{7/2}$ and W^0 $4f_{5/2}$ peaks at B.E. = 31.88 and 32.78 eV (Fig. 5d) also obtains the similar result for W 4f. On the basis of the CV tests, the $CoWO_4$ electrochemical process can be expected as the above reaction equations Eq. (1) and (2).

For $NiWO_4$, the reduction peaks of the first discharge process shift to ~1.3 and ~0.6 V, which is the characteristic behavior of the reduction of $NiWO_4$ to Ni(0), W(0), as can be explained by the reaction Eq. (3) [13–15, 28, 29, 33, 34]:

$$NiWO_4 + 8\,Li^+ + 8\,e^- \rightarrow Ni + W + 4\,Li_2O \quad (3)$$

And, in the anodic scan, two broad peaks at around 1.1–1.5 V correspond to reversible conversion of Ni and W into NiO and WO_3. In the subsequent cycles, the reduction peaks and oxidation peaks overlap at ~1.75 and ~0.25 V and ~1.1 and ~1.3 V, respectively, as shown in Eq. (4) [13–15, 28, 29, 33, 34]:

$$Ni + W + 4\,Li_2O \leftrightarrow NiO + WO_3 + 8\,Li^+ + 8\,e^- \quad (4)$$

On the basis of the research on the $CoWO_4$ electrode material, the XPS for $NiWO_4$ electrode material was implemented in Fig. 6. Figure 6a, b shows the XPS spectra of the fresh

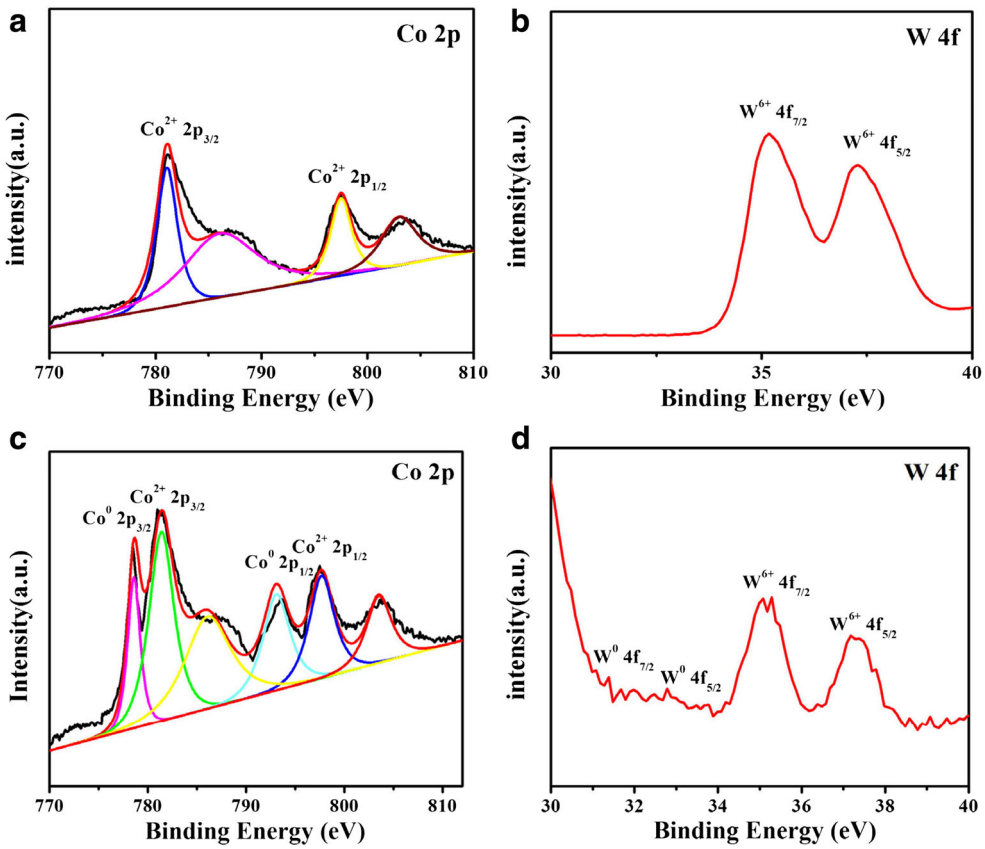

Fig. 5 Co 2p XPS spectrum of $CoWO_4$ (**a**). W 4f XPS spectrum of $CoWO_4$ (**b**). Co 2p XPS spectrum of $CoWO_4$ after one cycle (**c**). W 4f XPS spectrum of $CoWO_4$ after one cycle (**d**)

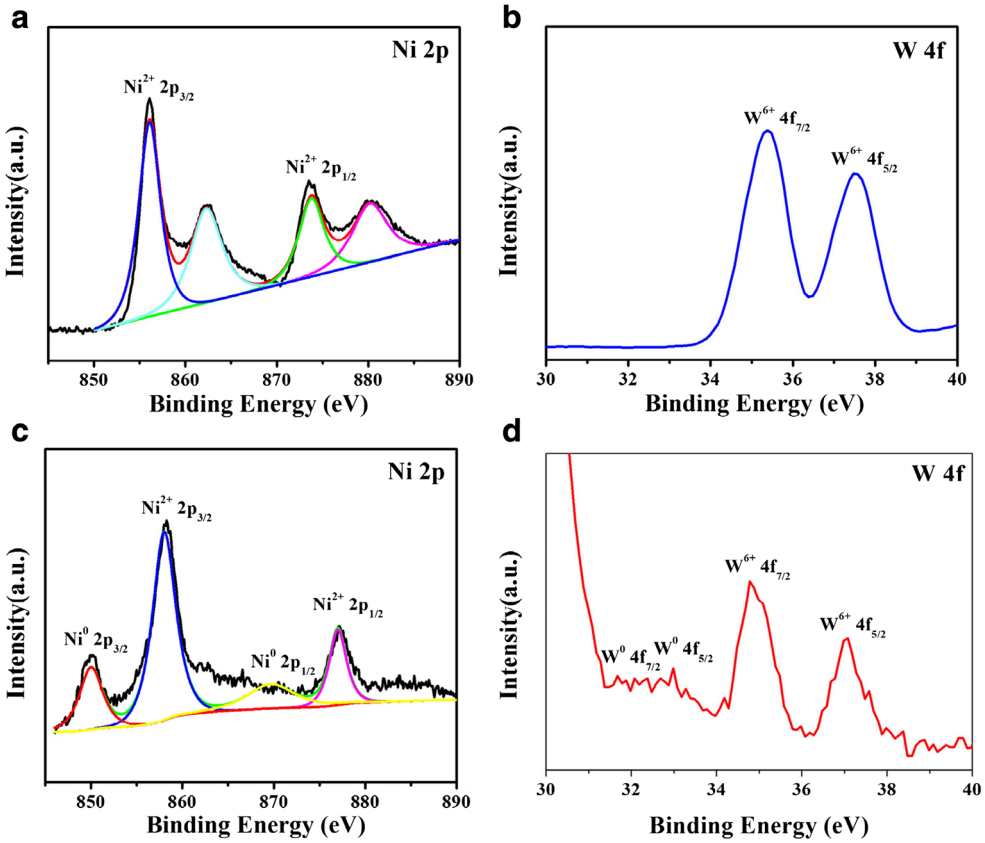

Fig. 6 Ni 2p XPS spectrum of $NiWO_4$ (**a**). W 4f XPS spectrum of $NiWO_4$ (**b**). Ni 2p XPS spectrum of $NiWO_4$ after one cycle (**c**). W 4f XPS spectrum of $NiWO_4$ after one cycle (**d**)

prepared electrode of the $NiWO_4$ nanoparticles. Two strong peaks at binding energies (B.E.s) = 856.08 and 873.78 eV are attributed to Ni^{2+} $2p_{3/2}$ and Ni^{2+} $2p_{1/2}$, respectively. The W 4f spectra shows two peaks at B.E. = 35.38 and 37.48 eV, corresponding to $4f_{7/2}$ and $4f_{5/2}$, respectively. These values of B.E.s also can be used to verify the as-synthesized $NiWO_4$ nanoparticles and indicate the elements of Ni and W exist in Ni^{2+} and W^{6+}, respectively [19, 20].

In order to clarify the electrochemical processes of $NiWO_4$ electrode during cyclic process, the ex-situ XPS were also tested after the electrode discharge/charge at a current density of 200 mA g^{-1} for one cycle. As shown in Fig. 6c, the peaks belonging to Ni $2p_{3/2}$ and Ni $2p_{1/2}$ change into two parts. The retention of the Ni^{2+} $2p_{3/2}$ and Ni^{2+} $2p_{1/2}$ peaks is due to the oxidation reaction of Ni in the charging process. Besides the existence of Ni^{2+}, two peaks at B.E. = 849.98 and 870.08 eV corresponding to the Ni^0 $2p_{3/2}$ and Ni^0 $2p_{1/2}$ state, which also can indicate that the Ni element exists partially in the metallic after one circle, and it also confirms that the oxidation process of the Ni element is incomplete because of high current density. Furthermore, the appearance of W^0 $4f_{7/2}$ and W^0 $4f_{5/2}$ peaks at B.E. = 31.48 and 32.88 eV (Fig. 6d) also obtains the similar result for W 4f. On the basis of the CV tests, the $NiWO_4$ electrochemical process also can be expected as above reaction Eqs. (3) and (4).

The electrochemical performance of the MWO_4 (M = Co, Ni) samples was also experimented by galvanostatic charge-discharge test, within the voltage window from 0.01 to 3 V (vs. Li/Li^+), at room temperature (25 °C). Figure 7a reveals the voltage curves of $CoWO_4$ electrode at a current density of 200 mA g^{-1} in the 1st, 2nd, 3rd, 5th, 10th, 15th, and until 120th cycle. In the first discharge curves, it is evident that three platforms are at about 1.25, 0.5, and 0.25 V, which is consistent with the results confirmed by the above CV test. The first discharge and charge capacities of $CoWO_4$ electrode are 1259.0 and 929.7 mA h g^{-1}, respectively, with an initial coulombic efficiency of 75.93%; the capacity loss is mainly due to the formation of SEI layer and some undecomposed Li_2O. In addition, it is observed that with the increasing number of cycles, the discharge curves gradually overlap and discharge capacity decreases first and then increases, which can be seen more clearly from Fig. 7b. As shown in Fig. 7b, the coulombic efficiency increased to above 99% after only 6 cycles, and the discharge capacities keep at about 880 mA h g^{-1}. More interestingly, the capacity of $CoWO_4$ electrode gradually increases after about 60 cycles; not only the coulombic efficiency stays above 99% but also the capacity reaches stable and still maintained a high reversible capacity of 980 mA h g^{-1} even after 120 cycles. The capacity rise phenomenon also widely occurs in various nanostructured metal-oxide electrodes [35–38], which is usually attributed to the

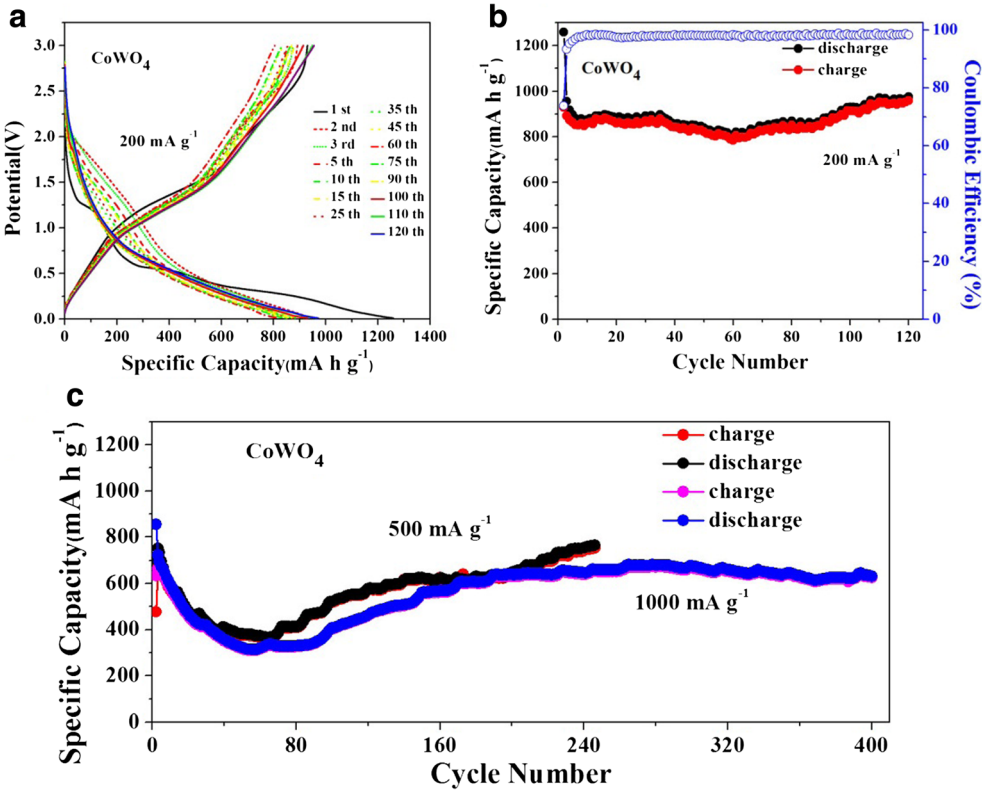

Fig. 7 Galvanostatic discharge/charge profiles of the $CoWO_4$ electrode (**a**). Cycling performance of the $CoWO_4$ electrode (**b**, **c**)

contribution of the activation of the electrode materials and the reversible formation/decomposition of the SEI film, which could deliver extra lithium interfacial storage at a low potential through a so-called "pseudo-capacitance-type" mechanism.

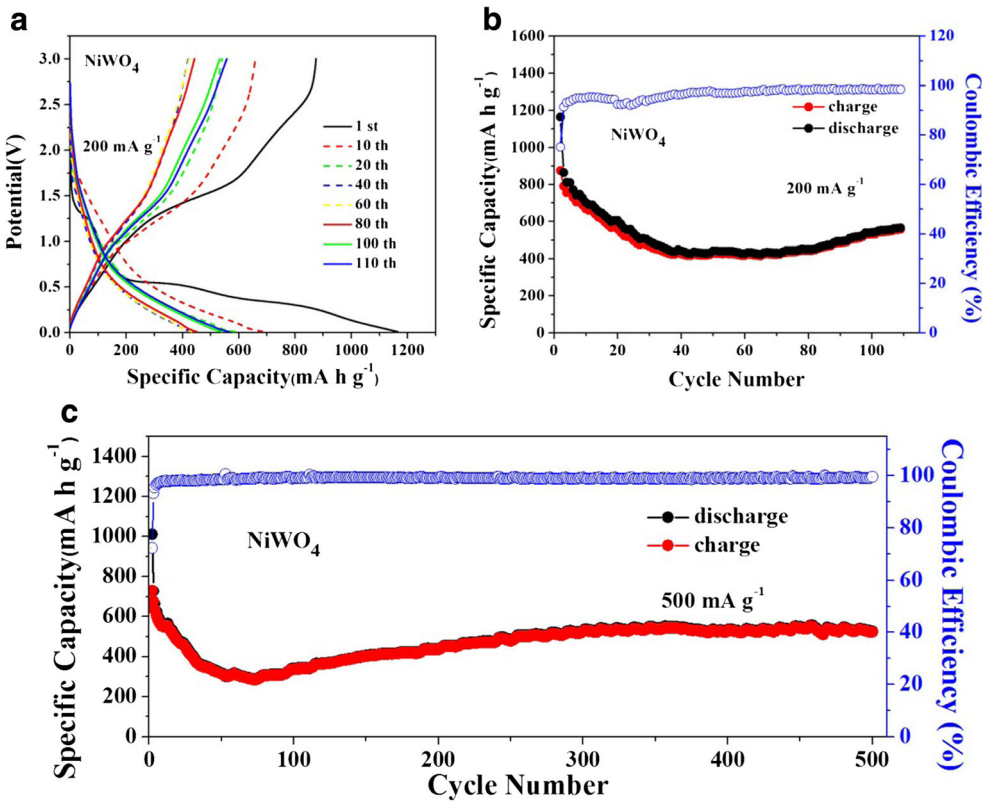

Fig. 8 Galvanostatic discharge/charge profiles of $NiWO_4$ electrode (**a**). Cycling performance of $NiWO_4$ electrode (**b**, **c**)

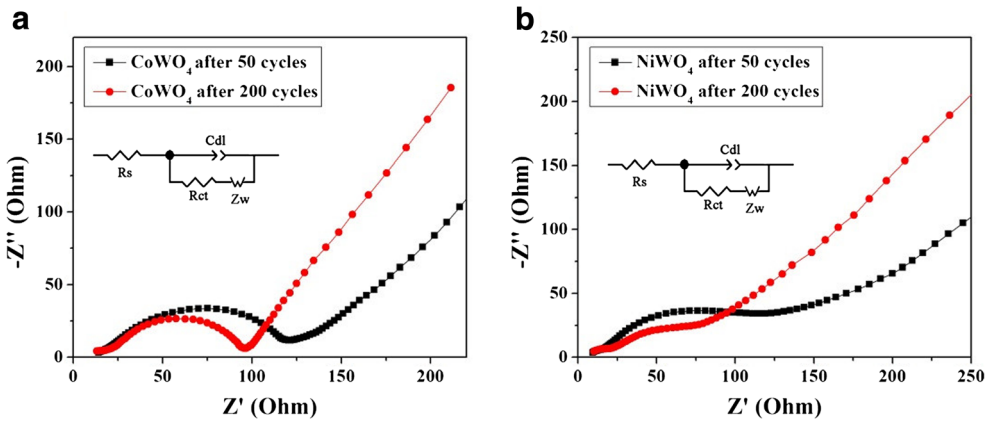

Fig. 9 The impedance spectra of $CoWO_4$ (**a**) and $NiWO_4$ (**b**) after 50 and 200 cycles

[39, 40] As shown in Fig. 7a, the extra capacity comes mainly from the contribution below 1.25 V, corresponding to the formation of a polymeric/gel-like layer. In addition, Na-alginate as high-efficient polymer binders with high elasticity and adhesivity is beneficial to maintain the electrode structure and the integrity of the conductive network [41–43], enhancing cycling performance of the high-capacity electrode. More cycling performance tests are shown in Fig. 7c at higher current density of 500 and 1000 mA g^{-1}; after similar short capacity decay, the reversible capacity also can increases to 752.3 mA h g^{-1} after 240 cycles and 632 mA h g^{-1} after 400 cycles, respectively, indicating the excellent cycling performance and rate capability.

The galvanostatic discharge/charge profile of $NiWO_4$ nanoparticles is shown in Fig. 8a; at a current density of 200 mA g^{-1}, the long platform of the discharge curves is in line with the results confirmed by above CV test (Fig. 4b). As shown in Fig. 8a, b, the discharge capacity of the 1st, 10th, 20th, 40th, 60th, 80th, 100th, and 110th cycles are 1164.6, 690.6, 585.9, 435.0, 432.9, 450.1, 541.4, and 565.8 mA h g^{-1}, respectively. It is revealed that the discharge capacity reduces in the front 60 cycles, and then slowly increases in the subsequent cycles. Interestingly, the similar capacity growth phenomenon also shows in the $NiWO_4$ electrode, which could be explained by the above reason [39–43]. Furthermore, the cyclic stability of $NiWO_4$ at a higher constant density of 500 mA g^{-1} is depicted in Fig. 8c, which also can deliver a stable discharge capacity of 542.1 mA h g^{-1} even after 500 cycles, also testifying the good cycle performance of $NiWO_4$ nanoparticles.

Figure 9 shows the Nyquist plots of $CoWO_4$ and $NiWO_4$ electrodes from 100 kHz to 0.01 Hz after 50 and 200 cycles at 500 mA g^{-1} to prove their good electrochemical performances. The equivalent circuit is displayed in the inset of Fig. 9a, b, where R_s is the SEI film and/or contact resistance; R_{ct} is the charge transfer resistance; C_{dl} is the capacitance related to the double layer, while Z_w represents Warburg impedance associated with Li-ion diffusion process within the electrode [44, 45]. The plots are composed of a semicircle at high-frequency area and oblique line at low-frequency area, which is corresponding to the charge-transfer resistance (R_{ct}) and Warburg impedance (Z_w), respectively [46–48]. Table 1 lists the R_{ct} parameters calculated from the equivalent circuit model. The slight change of Rs along with the increase of the cycle number could indicate the stability of SEI film in the cycling process. It is quite clear that the charge-transfer resistances (R_{ct}) of two electrodes after 200 cycles are much smaller than these of two electrodes after 50 cycles, indicating the improved kinetics along with cycle number. The decreased R_{ct} may be relevant to possible activation process in the electrodes, which facilitates contact between the active material and electrolyte, and improve the electronic conductivity of the integrated electrode [49], which also might be one reasonable explanation on capacity growth phenomenon.

The rate performances of $CoWO_4$ and $NiWO_4$ nanoparticles at various current rates from 0.1 to 1.6 A g^{-1} are exhibited in Fig. 10a, b, respectively. For $CoWO_4$ and $NiWO_4$, the average discharge capacities are 900, 850, 700, 600, and 580 mA h g^{-1} and 700, 600, 400, 300, and 250 mA h g^{-1}, at current density of 0.1, 0.2, 0.5, 1, and 1.6 A g^{-1}, respectively. In addition, after during continuous huge current measurement, when the rate is returned to 0.1 A g^{-1}, the capacities of $CoWO_4$ and $NiWO_4$ are still able to return to over 1000 and 700 mA h g^{-1}, respectively. The initial capacity could almost be regained and even exceed, which means the electrode structure keeps stable even through the diverse current density transition.

Table 1 Impedance parameters calculated from equivalent circuit model

	$CoWO_4$ (50th)	$CoWO_4$ (200th)	$NiWO_4$ (50th)	$NiWO_4$ (200th)
R_s (Ω)	11.4	14.3	10.2	12.1
R_{ct} (Ω)	106.1	82.6	195.9	44.0

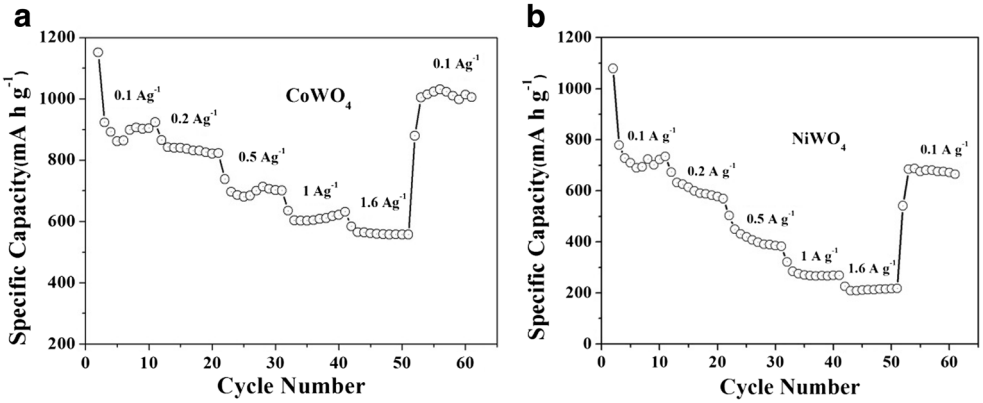

Fig. 10 Rate performance of $CoWO_4$ (**a**) and $NiWO_4$ (**b**) electrodes

From the above, the excellent lithium storage performance of $CoWO_4$ and $NiWO_4$ can be attributed to unique nanoparticles structure. On one hand, the compact packing structure of nanoparticles can reduce the transmission length of Li^+ ions and electrons, which effectively enhances battery reaction kinetics. On the other hand, two tungstate nanostructures with relatively uniform size and shape maintain the stability of the electrode structure by accommodating the volume expansion of electrode materials during Li^+ ion insertion and extraction process. In a word, the good rate capability and cycle performance of electrode material are attributed to the unique nanoparticle structure.

Conclusions

In summary, the $CoWO_4$ and $NiWO_4$ nanoparticles have been successfully synthesized via a facile one-step hydrothermal approach; the obtained nanoparticles exist relative uniform size and morphology. When tested as the novel anode materials for LIBs, both $CoWO_4$ and $NiWO_4$ nanoparticles reveal high capacity and good cycle performance. For the $CoWO_4$ electrode, a high reversible capacity of 980 mA h g^{-1} was obtained at 200 mA g^{-1} and the discharge capacity of 632 mA h g^{-1} remained at 1000 mA g^{-1} even after 400 cycles. Moreover, the discharge capacity of $NiWO_4$ electrode was still maintained at 542.1 mA h g^{-1} after 500 cycles. The excellent electrochemical performance was ascribed to the unique nanoparticle structure, which could effectively shorten the diffusion distance of Li^+ ions and electrons and alleviate the volume expansion of electrode materials during charge-discharge. Therefore, the superior electrochemical performance endowed the $NiWO_4$ and $CoWO_4$ nanoparticles with potential application for high-performance LIBs.

Acknowledgements This work was supported by the National Natural Science Foundation of China (no. 51362018) and the Foundation for Innovation Groups of Basic Research in Gansu Province (no. 1606RJIA322).

References

1. Liu C, Li F, Ma LP, Cheng HM (2010) Advanced materials for energy storage. Adv Mater 22:E28–E62
2. Choi D, Cartmell S, Han K, Huang Q, Thomsen E, Xu W, Sprenkle V (2016) Electrochemical and structural investigations of titanate based anodes for high power and long cycle life li-ion battery. ECS Mee Abs 3:2151–2041
3. Whittingham MS (2008) Inorganic nanomaterials for batteries. Dalton Trans 40:5424–5431
4. Chen YA, Fu K, Zhu SZ, Luo W, Wang YB, Li YJ, Hitz E, Yao YG, Dai JQ, Wan JY, Danner VA, Li T, Hu LB (2016) Reduced graphene oxide films with ultrahigh conductivity as li-ion battery current collectors. Nano Lett 16:3616–3623
5. Kim WS, Hwa Y, Kim HC, Choi JH, Sohn HJ, Hong SH (2014) SnO_2@Co_3O_4 hollow nano-spheres for a Li-ion battery anode with extraordinary performance. Nano Res 7:1128–1136
6. Larcher D, Tarascon JM (2015) Towards greener and more sustainable batteries for electrical energy storage. Nat Chem 7:19–29
7. Risacher F, Fritz B (2009) Origin of salts and brine evolution of Bolivian and Chilean salars. Aquat Geochem 15:123–157
8. Wang YK, Chen J, Jiang CC, Ding NW, Wang CX, Li D, Liu XL, Zhong Q, Li ZF, Zhong SW (2016) Tetra-β-nitro-substituted phthalocyanines: a new organic electrode material for lithium batteries. J Solid State Eelectrochem 10:1432–8488
9. Wilken A, Kraft V, Girod S, Winter M, Nowak S (2016) A fluoride-selective electrode (Fse) for the quantification of fluoride in lithium-ion battery (lib) electrolytes. Anal Methods 8:6932–6940
10. Chao DL, Xia XH, Liu JL, Fan ZX, Ng CF, Lin JY, Zhang H, Fan Fan HJ (2014) A V_2O_5/conductive-polymer core/shell nanobelt array on three-dimensional graphite foam: a high-rate, ultrastable, and freestanding cathode for lithium-ion batteries. Adv Mater 26:5794–5800
11. Cho JS, Hong YJ, Kang YC (2015) Design and synthesis of bubble-nanorod-structured Fe_2O_3-carbon nanofibers as advanced anode material for li-ion batteries. ACS Nano 9:4026–4035
12. Obrovac MN, Chevrier VL (2014) Alloy negative electrodes for li-ion batteries. Chem Rev 23:11444–11502
13. Gong C, Bai YJ, Feng J, Tang R, Qi YX, Lun N, Fan RH (2013) Enhanced electrochemical performance of $FeWO_4$ by coating nitrogen-doped carbon. ACS Appl Mater Interfaces 5:4209–4215
14. Shim HW, Lim AH, Kim JC, Lee GH, Kim DW (2013) Hydrothermal realization of a hierarchical, flowerlike $MnWO_4$@MWCNTs nanocomposite with enhanced reversible Li storage as a new anode material. Chem Asian J 8:2851–2858
15. Zhang E, Xing Z, Wang J, Ju ZC, Qian YT (2012) Enhanced energy storage and rate performance induced by dense nanocavities inside $MnWO_4$ nanobars. RSC Adv 2:6748–6751

16. Zhang LS, Wang ZT, Wang LZ, Xing Y, Li XF, Zhang Y (2014) Electrochemical performance of $ZnWO_4$/CNTs composite as anode materials for lithium-ion battery. J Mater Sci 305:179–185
17. Hitoki G, Takata T, Ikeda S, Hara M, Kondo JN, Kakihana M, Domen K (2000) Mechano-catalytic overall water splitting on some mixed oxides. Catal Today 63:175–181
18. Pullar RC, Farrah S, Alford NM (2007) $MgWO_4$, $ZnWO_4$, $NiWO_4$ and $CoWO_4$ microwave dielectric ceramics. J Eur Ceram Soc 27: 1059–1063
19. Srirapu VKVP, Kumar A, Srivastava P, Singh RN, Sinha ASK (2016) Nanosized $CoWO_4$ and $NiWO_4$ as efficient oxygen-evolving electrocatalysts. Electrochim Acta 209:75–84
20. Kumari N, Singh RN (2016) Nanocomposites of nitrogen-doped graphene and cobalt tungsten oxide as efficient electrode materials for application in electrochemical devices. AIMS Mater Sci 3: 1456–1473
21. Xu XY, Gao JP, Huang GB, Qiu HX, Wang ZY, Wu JZ, Pan Z, Xing FB (2015) Fabrication of $CoWO_4$@$NiWO_4$ nanocomposites with good supercapacitve performances. Electrochim Acta 174:837–845
22. He GJ, Li JM, Li WY, Li B, Noor N, Xu K, Hu JQ, Parkin IP (2015) One pot synthesis of nickel foam supported self-assembly of $NiWO_4$ and $CoWO_4$ nanostructures that act as high performance electrochemical capacitor electrodes. J Mater Chem A 3:14272–14278
23. Yin LX, Chai SM, Wang FF, Huang JF, Li JY, Liu CQ, Kong XG (2016) Ultrafine SnO_2 nanoparticles as a high performance anode material for lithium ion battery. Ceram Int 42:9433–9437
24. Li ZH, He Q, He L, Hu P, Li W, Yan HW, Peng XZ, Huang CY, Mai LQ (2017) Self-sacrificed synthesis of carbon-coated SiO_x nanowires for high capacity lithium ion battery anodes. J Mater Chem A 5:4183–4189
25. Yu L, Xia BY, Wang X, Lou XW (2015) General formation of M-MoS_3 (M = Co, Ni) hollow structures with enhanced electrocatalytic activity for hydrogen evolution. Adv Mater 28:92–97
26. Luo JS, Xia XH, Luo YS, Guan C, Liu JL, Qi XY, Ng CF, Yu T, Zhang H, Fan HJ (2013) Rationally designed hierarchical TiO_2@Fe_2O_3 hollow nanostructures for improved lithium ion storage. Adv Energy Mater 3:737–743
27. Guo YG, Hu JS, Wan LJ (2008) Nanostructured materials for electrochemical energy conversion and storage devices. Adv Mater 20: 2878–2887
28. Sasidharan M, Gunawardhana N, Yoshio M, Nakashima K (2012) WO_3 hollow nanospheres for high-lithium storage capacity and good cyclability. Nano Energy 1:503–508
29. Tong H, Xu YM, Cheng XL, Zhang XF, Gao S, Zhao H, Huo LH (2016) One-pot solvothermal synthesis of hierarchical WO_3 hollow microspheres with superior lithium ion battery anode performance. Electrochim Acta 210:147–154
30. Kang Q, Cao LY, Li JY, Huang JF, Xu ZW, Cheng YY, Wang X, Bai JY, Li QY (2016) Super P enhanced CoO anode for lithium-ion battery with superior electrochemical performance. Ceram Int 42: 15920–15925
31. Huang GY, Xu SM, Yang Y, Chen YB, Li ZB (2015) Rapid-rate capability of micro-/nano-structured CoO anodes with different morphologies for Lithium-ion batteries. Int J Electrochem Sci 10: 10587–10596
32. Yang G, Cui H, Yang G, Wang C (2014) Self-assembly of $Co_3V_2O_8$ multilayered nanosheets: controllable synthesis, excellent li-storage properties, and investigation of electrochemical mechanism. ACS Nano 8:4474–4487
33. Chen CH, Perdomo PJ, Fernandez M, Barbeito A, Wang CL (2016) Porous NiO/graphene composite thin films as high performance anodes for lithium-ion batteries. J Energy Storage 8:198–204
34. Cao W, Hu AP, Chen XH, Liu XH, Liu XH, Liu P, Tang QL, Zhao XS (2016) NiO hollow microspheres interconnected by carbon nanotubes as an anode for lithium ion batteries. Electrochim Acta 213:75–82
35. Zhu T, Chen JS, Lou XW (2011) Glucose-assisted one-pot synthesis of FeOOH Nanorods and their transformation to Fe_3O_4@carbon Nanorods for application in lithium ion batteries. J Phys Chem C 115:9814–9820
36. Ban C, Wu ZC, Gillaspie DT, Chen L, Yan Y, Blackburn JL, Dillon AC (2010) Nanostructured Fe_3O_4/SWNT electrode: binder-free and high-rate li-ion anode. Adv Mater 22:E145–E149
37. Xie KW, Yin JW, Shi HM, Zhu QY, Wu P, Tang YW, Lu TH (2015) Designed synthesis of NiO@polypyrrole hollow spheres for long-life lithium storage. Ionics 21:359–364
38. Sun KL, Zhao HB, Yao HA, Zhang SQ, Xu JX (2014) Foam carbon loading Fe_3O_4 nanoparticles for superior lithium-ion batteries anode material. Ionics 21:1901–1908
39. Wang Z, Luan D, Madhavi S, Hu Y, Lou XWD (2012) Assembling carbon-coated α-Fe_2O_3 hollow nanohorns on the CNT backbone for superior lithium storage capability. Energy Environ Sci 5:5252–5256
40. Zhang N, Zhao Q, Han X, Yang J, Chen J (2014) Pitaya-like Sn@C nanocomposites as high-rate and long-life anode for lithium-ion batteries. Nano 6:2827–2832
41. Kovalenko I, Zdyrko B, Magasinski A, Hertzberg B, Milicev Z, Burtovyy R, Luzinov I, Yushin G (2011) A major constituent of Brown algae for use in high-capacity Li-ion batteries. Science 334: 75–79
42. Ge MY, Rong JP, Fang X, Zhou CG (2012) Porous doped silicon nanowires for lithium ion battery anode with long cycle life. Nano Lett 12:2318–2323
43. Li JX, Zhao Y, Wang N, Ding YH, Guan LH (2012) Enhanced performance of a MnO_2-graphene sheet cathode for lithium ion batteries using sodium alginate as a binder. J Mater Chem 22: 13002–13004
44. Li Y, Kong LB, Liu MC, Zhang WB, Kang L (2017) Facile synthesis of $Co_3V_2O_8$ nanoparticle arrays on Ni foam as binder-free electrode with improved lithium storage properties. Ceram Int 43: 1166–1173
45. Xiang JY, Tu JP, Qiao YQ, Wang XL, Zhong J, Zhang D, Gu CD (2011) Electrochemical impedance analysis of a hierarchical CuO electrode composed of self-assembled nanoplates. J Phys Chem C 115:2505–2513
46. Shen XY, Mu DB, Chen S, Wu BR, Wu F (2013) Enhanced electrochemical performance of ZnO-loaded/porous carbon composite as anode materials for lithium ion batteries. ACS Appl Mater Interfaces 8:3118–3125
47. Huang G, Xu S, Lu S, Li L, Sun H (2014) Micro-/nanostructured Co_3O_4 anode with enhanced rate capability for lithium-ion batteries. ACS Appl Mater Interfaces 6:7236–7243
48. He CN, Wu SH, Zhao NQ, Shi CS, Liu EZ, Li JJ (2013) Carbon-encapsulated Fe_3O_4 nanoparticles as a high-rate lithium ion battery anode material. ACS Nano 5:4459–4469
49. Ni SB, Ma JJ, Zhang JC, Yang XL, Zhang LL (2015) The electrochemical performance of commercial ferric oxide anode with natural graphite adding and sodium alginate binder. Electrochim Acta 153:546–551